Numerical Studies of Object Localisation Using Ocean Acoustic Tomography

[*] Michaela Murzyniec † Ireneusz Czajka
*German Aerospace Center (DLR), Institute for the Protection of Maritime Infrastructures, Germany
†AGH University of Krakow, Poland

***Abstract*—Ocean acoustic tomography (OAT) is a technique used to study ocean properties by analysing sound wave propagation. In this study, OAT is used to detect and localise underwater objects by analysing variations in acoustic wave propagation caused by their presence. This paper explores the application of acoustic tomography for underwater object localisation through numerical modeling. Using COMSOL Multiphysics and the finite element method, a two-dimensional harbour model is developed, incorporating an acoustic monopole as a sound source, forty hydrophones, and a rectangular object. The study analyses the impact of object positioning on acoustic pressure distribution in both time and frequency domains. The results indicate that hydrophones located close to or nearby an object's position show visible anomalies, captured both in time signals and frequency-amplitude spectra. Similar patterns were observed for certain positions of hydrophones, whereas receivers located farther from the object did not capture any significant differences.**

***Index Terms*—ocean acoustic tomography, finite element method, passive localisation, object detection**

I. Introduction

Ocean acoustic tomography (OAT) used for environmental monitoring provides detailed information about the area being surveyed and can indirectly be used to determine the location of unknown underwater objects using already deployed hydrophone arrays to detect pressure anomalies or suspicious activities therefore improving safety and security of the studied areas. This secondary application makes OAT an extremely useful technique both in security and environmental research. In oceanographic studies, traditional in situ methods such as CTD (Conductivity, Temperature, Depth) probes and Argo floats provide accurate data but are limited by depth and receiver spacing [1]–[5]. Satellite remote sensing offers broader coverage, providing information on surface temperature, sea level, and chemical compounds on the sea surface, however, it struggles to access subsurface data, especially in harsh atmospheric conditions [6]–[8]. As a complementary technique, OAT - inspired by medical and seismic tomography, introduced by W. Munk and C. Wunsch in the late 1970s [9], enabled studies of large ocean areas followed by multiple measurement campaigns [10]–[13]. In principle, OAT explores the relationship between sound speed and parameters such as temperature, salinity, and pressure. By accurately measuring the time of flight (TOF) of acoustic signals between distant sources and receivers, it is possible to calculate average sound speed and reconstruct temperature profiles, ocean currents, and pressure changes [14], [15]. In practice, oceanographers deploy arrays of multiple sound sources and receivers, enabling the use of numerous source-receiver paths to gather detailed spatial information about the ocean's interior [16], [17].

After World War II, fixed hydrophone arrays such as the U.S. Navy's Sound Surveillance System (SOSUS) were used to detect submarines over long distances in the deep ocean using low frequency acoustic signals and special propagation channels as a part of early warning operations [18]. This project is related at a conceptual level - a hydrophone array is placed within a harbour environment, even though detection in this setting poses challenges. Deploying sensors near harbour entrances or maritime borders and combining them with other underwater systems including sonars, multibeam, autonomous vehicles or distributed fibre-optic sensing could provide a clearer picture of underwater activity. Since the harbour environment is characterised by shallow, noisy and highly reverberant conditions, it requires a detailed simulation setup. The motivation for this study is to investigate changes in pressure-field caused by the presence of an object using a dense hydrophone array and numerical calculations.

To support OAT measurements and parameter reconstruction, modeling the pressure field is essential and commonly performed using finite element method (FEM), boundary element method (BEM), or geometric methods such as ray tracing (RT). FEM, widely used in engineering, solves complex partial differential equations by discretising the domain and interpolating solutions with polynomial basis functions at nodal points, assembling these into a global system solved using linear algebra. FEM is especially useful for analysing acoustic fields and wave propagation in heterogeneous, closed domains with complex geometry. Nevertheless, due to the fine discretisation required for accuracy particularly at high frequencies, FEM is considered as computationally demanding. Compared to FEM, BEM is less resource-intensive because it discretises only the boundary, reducing system size and computational cost, and is effective for open, infinite domains with homogeneous media [19]–[21]. Geometric methods, meanwhile, offer high accuracy for large closed domains with lower computational demands, where the size of the domain exceeds the wavelength significantly. However, they simplify wave phenomena by treating acoustic waves as rays, which travel through homogeneous media in straight lines with wave scattering performed according to Snell's Law. Moreover, RT does not include wave diffraction and other complex wave phenomena [22], [23].

Once the acoustic field is modelled and TOF data are obtained, special algorithms such as SIRT (Simultaneous Iterative Reconstruction Technique), ART (Algebraic Reconstruction Technique), Conjugated Gradient method or SAFT (Synthetic Aperture Focusing Technique), FDFD (Finite Difference Frequency Domain) or f-k (Frequency Wavenumber Migration Algorithm) can be performed both in frequency and time domain to reconstruct spatial information [24]–[28].

Within this work, FEM is used to model the sound pressure field inside the 2D harbour model designed in COMSOL Multiphysics with 40 hydrophones, a static sound source and a rectangular object placed in nine positions used as a scattering obstacle. Since the main goal was to study the behaviour of the pressure field throughout the domain rather than only at boundaries, FEM was more suitable, allowing easier extraction of TOF information, whereas BEM, typically preferred for open-domain problems, primarily provides solutions on object or domain boundaries. OAT is used to capture TOF in multiple source-receiver paths between all deployed receivers. Analysis is performed both in time domain, where generalised cross correlation (GCC) is used to calculate and study time delays based on TOF, and frequency domain where power spectra obtained from each source-receiver pair are discussed. The study compares no-object scenario with scenarios where object is positioned in each of nine positions. This research shows how FEM-based modelling in a 2D harbour can reveal pressure changes caused by different object positions, taking a step toward practical use of OAT in harbour monitoring.

II. Design of the harbour model

A two-dimensional harbour geometry is constructed within an unrestricted water basin, with edges defining the simulation domain. The top, left, and right edges use perfectly matched layers (PMLs) to prevent artificial wave reflections, ensuring an infinite water domain effect. The bottom edge of the domain, representing the harbour boundary, is modelled as a rigid wall with a Neumann boundary condition, causing full wave reflection. Similarly, internal edges including harbour structure and the scattering object, are modelled with the Neumann boundary condition, ensuring that waves reflect off these surfaces while allowing for natural scattering and diffraction within the domain. Limiting the harbour with edges resulted in a computational domain with dimensions of 10 m$\times$12.5 m, balancing accuracy with computational efficiency. The harbour geometry is shown on Fig. 1. Inside the water basin a sound source is modelled as an acoustic monopole with a sound pressure level of 165 dB relative to 1μPa at 1 kHz with a radius of 0.3 m, and 40 receivers are placed in a uniform grid with a spacing of 1.5 m. The center of the sound source is placed at an equal distance between the receivers numbered p13, p14, p21, p22. In addition, a rectangular scattering object with dimensions of 1.5 m$\times$0.75 m, is placed at nine positions. Ten scenarios are considered. The first simulation examines the propagation of acoustic waves when the object is not present in the basin. The simulation adopts a linear model of water medium, in which attenuation, which would result in pressure changes, is not taken into account. This model

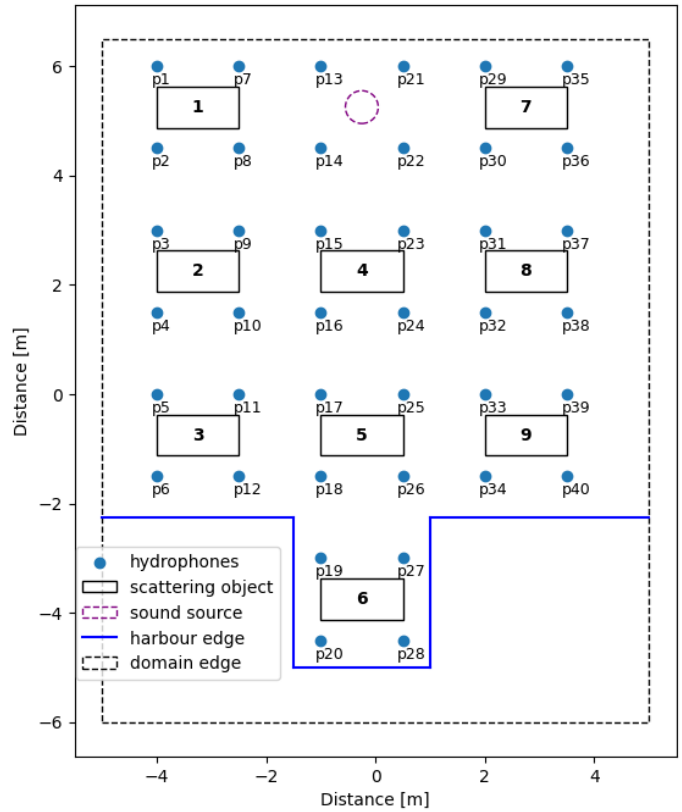

Fig. 1. Top view of the 2D harbour model in xy plane used for COMSOL Multiphysics simulations. The sound source is marked as dotted circle. The numbered boxes (1–9) indicate the positions of the scattering object in different scenarios. The blue line at the bottom represents the edge of the harbour.

assumes the presence of only linear acoustic phenomena and thus reflects an idealised hydrophone array deployment in the water column. The speed of sound and the density of the medium are taken as $c = 1500$ m/s and $\rho = 1000$ kg/m^3.

III. Scope of calculations

Frequency-domain FEM simulations are performed for each object position and in the absence of the object, covering a frequency range of 1–10 kHz. The selected range is determined by the scattering object's dimensions (1.5 m$\times$0.75 m); at 2 kHz, the wavelength in water is comparable to the object's smaller dimension, ensuring adequate resolution of scattering effects. The lower limit is extended to 1 kHz to account for low-frequency interactions and diffraction phenomena that influence wave propagation. For mesh construction, 5 elements are arranged at the shortest wavelength (for $f = 10$ kHz) resulting in fixed mesh refinement for considered frequency range. The obtained dataset contains complex pressure values recorded by each of the 40 receivers for each object's position. Subsequently, inverse Fourier transform (IFFT) is performed which provides signals in the time domain. Time delays of signals between pairs of receivers are calculated on the basis of GCC [29], [30]. The signal at the receiver i in the time domain

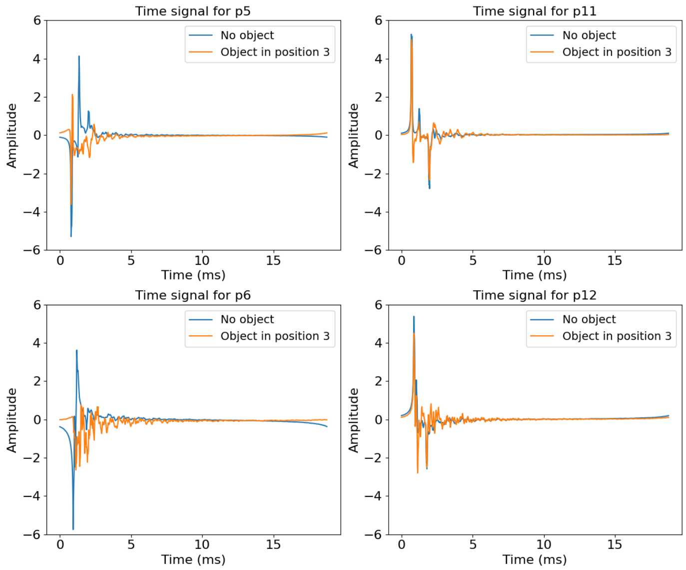

Fig. 2. Comparison between time domain signals obtained for hydrophones p5, p6, p11, p12 with object in position 3 and no-object scenario. Blue line represents reference signal for each hydrophone p5, p6, p11, p12 with no object present in computational domain. Orange line presents time signal when object is located in position 3 for each of considered hydrophones. Hydrophones p5, p6, p11, p12 remain closest to object's position 3.

can be modelled as original time signal $s(t)$ with additive noise n_i:

$$s_i(t) = s(t) + n_i(t), \tag{1}$$

and the delayed version of the time signal at the receiver j as

$$s_j(t) = s(t - \tau ij) + n_j(t), \tag{2}$$

where τ is time delay between two receivers.

In the frequency domain GCC-PHAT function is described as

$$R_{s_i s_j}(\tau) = \int_{-\infty}^{+\infty} \phi_{PHAT}(f) G_{s_i s_j}(f) e^{j2\pi f \tau_{ij}} df, \tag{3}$$

with $G_{s_i s_j}(f) = S_i(f) S_j(f)^*$ the cross-spectral density, $S_i(f)$ the Fourier transform of s_i, and $\phi_{PHAT}(f) = \frac{1}{|G_{s_i s_j}(f)|}$ enhances robustness against noise and reverberation.

The estimated time delay is obtained as

$$\hat{\tau_{ij}} = \arg\max_{\tau_{ij}} R_{s_i s_j}(\tau_{ij}). \tag{4}$$

IV. Results

Analysis is performed both in the time domain and frequency domain. Time domain signals are visible in Fig. 2 and Fig. 3. Fig. 2 compares signals obtained for receivers p5, p6, p11, p12 for the object-free scenario and when the object is located in position 3, for which those receivers are the closest. We can observe that shadowed hydrophone,

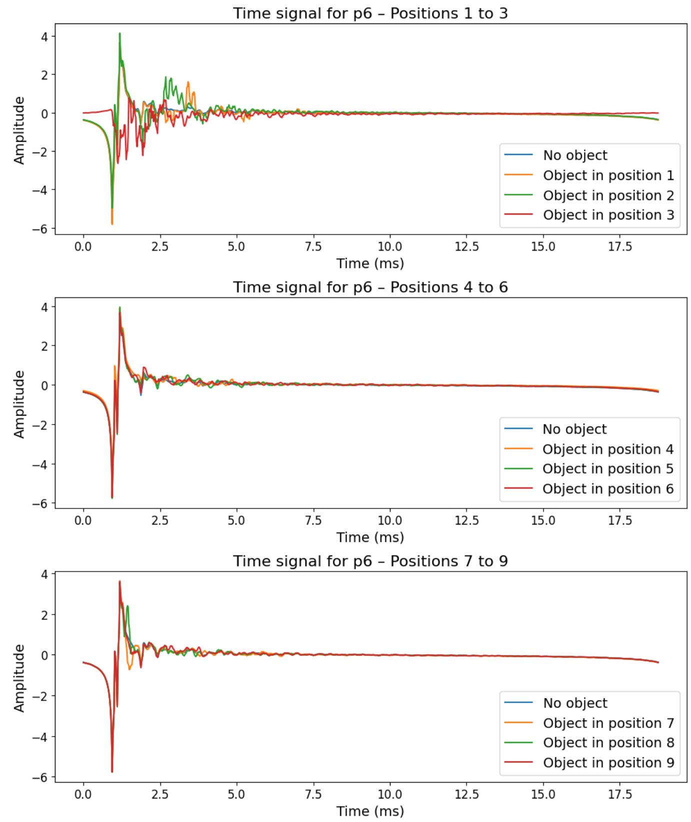

Fig. 3. Time-domain signals obtained for all considered positions of the object 1 to 9 for hydrophone p6. Blue line shows time-signal for p6 when object is not present in the domain. Remaining colours represent time signal for p6 for specific position of the object.

p6, exhibits visible amplitude dampening and multiple peaks with smaller amplitude around impulse-peak when the object is present, whereas exposed p11 being close to the object resembles the reference signal curve (the object-free scenario) very strongly. Hydrophones p5, and p12 are not directly shadowed by the object in position 3, nevertheless they showcase visible irregularities probably caused by wave diffraction on the edge of the object. Fig. 3 shows comparison between all considered positions of the object for time signal recorded by the hydrophone p6. It is clear that, position 3 affects the signal curve most significantly because there p6 is shadowed by the object, whereas for positions 4 to 9 the signal curve corresponds to reference curve (the object-free scenario) very well. Similarly for positions 1 and 2 we observe that the signal curve for the impulse peak resembles the reference curve quite well however around 2.5 ms additional peaks occur presumably as a result of wave scattering from the object.

In order to showcase the time-delays, four heatmaps treating p5, p6, p11 and p12 as reference are shown in the Fig. 4. Here, we observe that p5 shows high negative delays for all other receivers when the object is at position 2, while p6 shows similar trends for positions 2 and 3. This happens because the object shadows p5 at position 2, blocking the direct path between source and p5. For p6, the direct path

DOI: 10.5281/zenodo.17120138

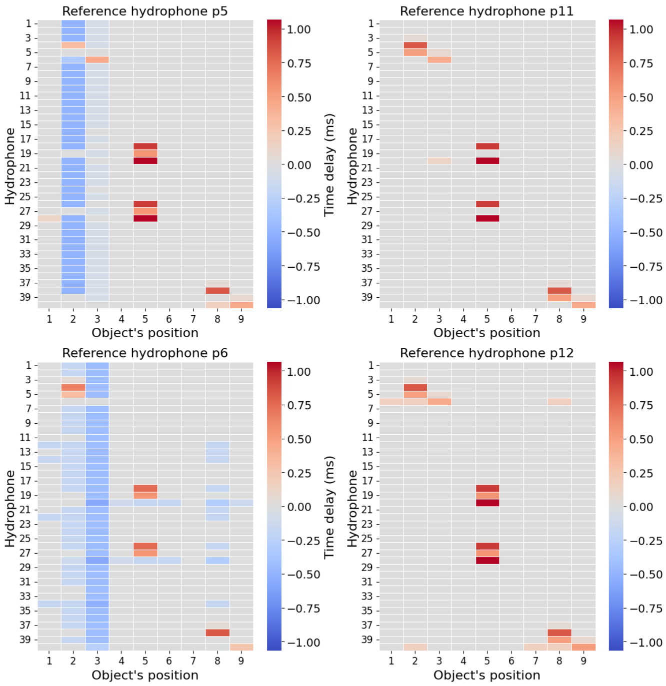

Fig. 4. Time-delay heatmaps obtained for p5, p6 and p11, p12 treated as reference. x-axis corresponds to the object's position and y-axis shows the hydrophone number. Each hydrophone is compared to reference hydrophone. Time delays are presented by gradient colours between red and blue. Blue colour represents negative time delay and indicates that compared hydrophone received signal earlier than reference. Red colour represents positive time delays and shows that compared hydrophone received signal later than reference.

is blocked at position 3 and affected (yet not fully blocked) at position 2. Consequently, p5 and p6 experience negative delays as they are shadowed, causing other receivers to record the signal earlier than the reference. Treating p11 and p12 as references, positive delays are observed for hydrophones shadowed along the direct source-receiver path such as p4-p6 at positions 2 and 3, p18-p20 and p26-p28 at position 5, and p38-p40 at positions 8 and 9. When object is located in position 5, 8 or 9 similar observations are noticed in case of p5 and p6 when treated as reference. Additional positive delays can be a result of scattering from the harbour edge or the object edge. Within this work, each of 40 receivers is treated as a reference so that we can observe the behaviour of the pressure field from different perspectives in order to perform reconstruction algorithms in future research, but only p5, p6, p11, p12 and p14 are chosen to showcase the observations as they show similar trends based on their positioning. Fig. 5 shows nine scatter plots obtained for all object positions, using hydrophone p14 as a reference which is positioned nearby the sound source. The largest positive time delays occur at hydrophones shadowed by the object and in close proximity to it, while those shadowed but farther away exhibit smaller time-delays. Hydrophones not shadowed yet close to the object show near-zero delays, confirming that the time-delay analysis can aid in preliminary object localisation.

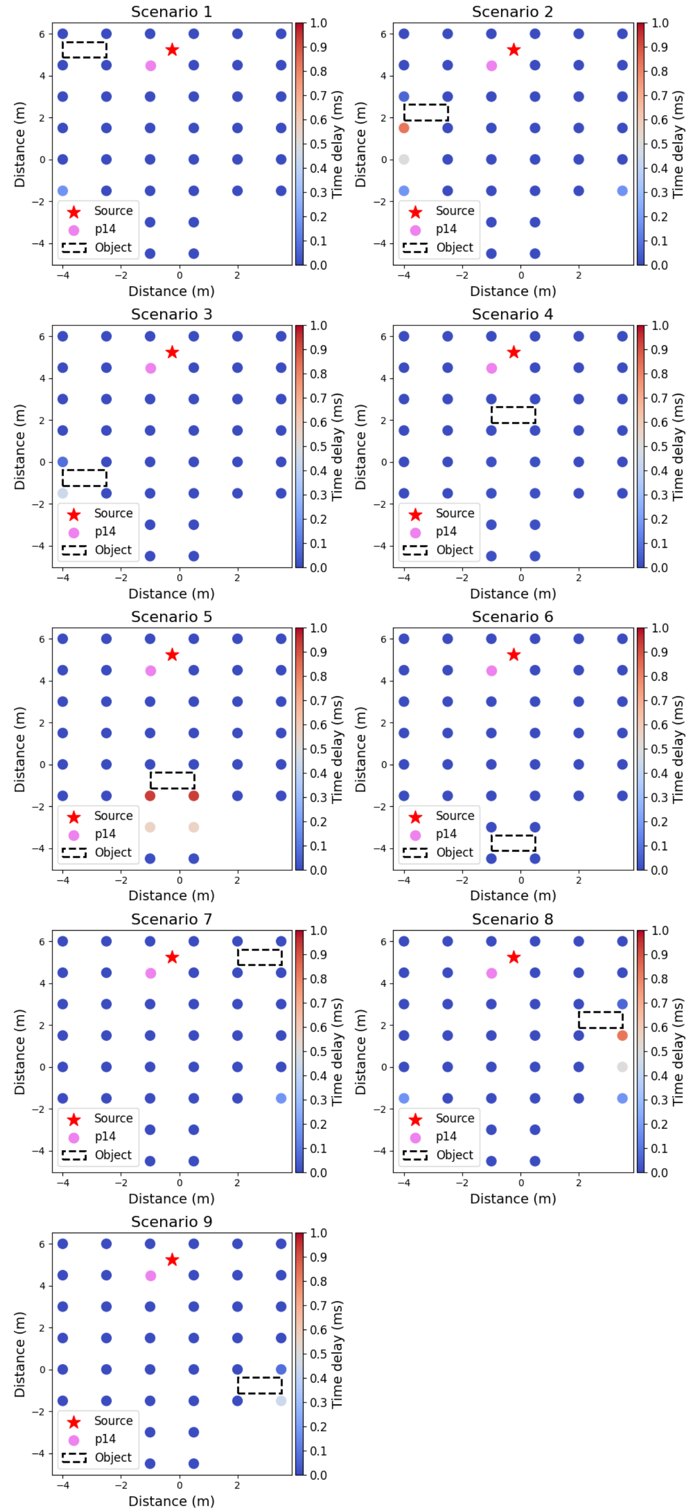

Fig. 5. Scatter plots of the time delays obtained for each analysed object position relative to the reference hydrophone p14 based on GCC. The reference hydrophone p14 is marked in pink and it is positioned on the top close to the sound source represented by a red star. The object's position in each scenario is indicated by a black dashed outline. Each dot corresponds to a hydrophone position, with its colour representing the time delay (in ms) relative to p14. Blue indicates time delays close to 0, while red indicates positive time delays. A positive value indicates that compared hydrophone detects the signal later than reference p14.

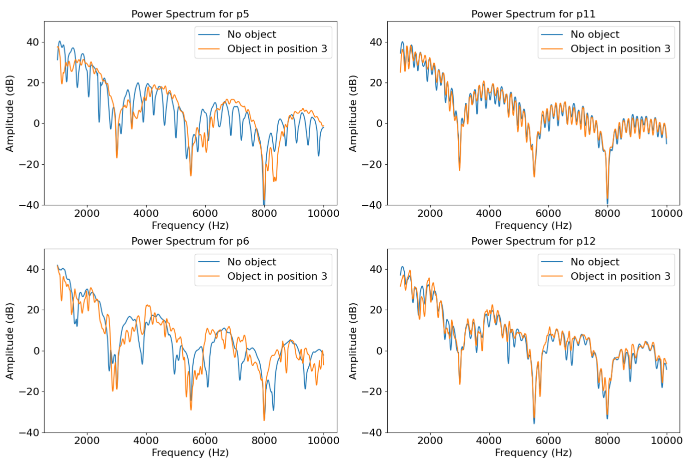

Fig. 6. Comparisons between power spectra obtained for hydrophones p5, p6, p11, p12 for no-object scenario (blue line) and when the object is located in position 3 (orange line). x-axis shows frequency from 1 to 10 kHz and y-axis shows amplitude in dB.

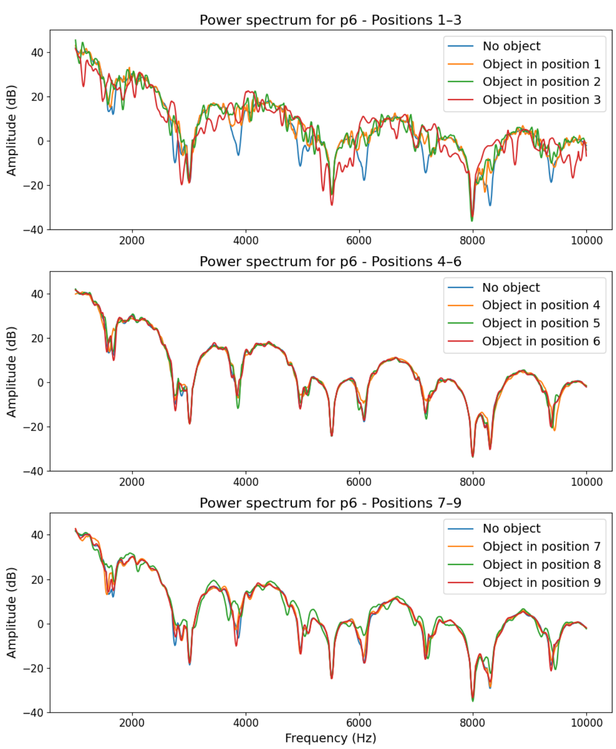

Fig. 7. Comparisons between power spectra obtained for hydrophone p6 for all object's positions 1 to 9 and no-object scenario. Blue line represents reference spectra for no object present in computational domain whereas remaining colours correspond with specific object's positions. x-axis shows frequency from 1 to 10 kHz and y-axis shows amplitude in dB.

In the frequency domain spectral analysis is performed focusing on power spectra obtained for every receiver. Again, analysis results in similar trends for certain hydrophone positions, therefore for clarity only some of them are shown. Fig. 6 shows power spectra obtained for signal recorded by hydrophone p5, p6, p11 and p12 comparing reference scenario to scenario with the object in position 3. The most significant irregularities are observed for shadowed hydrophone p6 whereas spectrum for exposed p11 aligns with the reference spectrum very well. Surprisingly, p12 spectrum curve corresponds sufficiently despite its close proximity to harbour edge and the object which could be the reason for noticeable wave scattering nevertheless, some irregularities are visible. Reference spectra between exposed p5, p11 and shadowed p6, p12 differ in shape particularly in case of spectra peaks, those hydrophones (p6, p12) located close to the hard boundary wall (harbour edge) showcase spectra peaks as more irregular presumably as a result of strong wave reflection, compared to spectra obtained for p5 and p11. Extended studies which compare reference power spectra for all hydrophones showcase smoother shapes of spectra peaks for hydrophones located close to the sound source whereas spectra peaks for hydrophones located closer to harbour walls exhibit more distorted peaks. For all considered hydrophones local maxima and local minima occur for similar frequencies and the amplitude remains on the similar level. Fig. 7 compares power spectra obtained for hydrophone p6 for the object positions 1 to 9 and for the object-free scenario. When the object is present especially in positions 1 to 3, this significantly affects p6 power spectra because in those positions hydrophone is either shadowed (positions 2 and 3) or the reflected wave from the object most likely reaches p6 faster than the direct one (position 1). For remaining positions 4 to 9, where p6 is not located close to the object power spectra corresponds almost perfectly to the reference curve. Between all positions of the object and no-object cases we do not observe major shifts in location of spectra local maxima and minima as well as significant amplitude differences.

V. Conclusions

This work analysed how the presence and location of an object affect the simulated pressure field of a 2D harbour model in both time and frequency domains. Using a dense hydrophone array and multiple object positions enables a detailed analysis of pressure anomalies. The results indicate that hydrophones located near or shadowed by the object exhibit the most visible irregularities both in time and frequency domain. Understanding the pressure field in an object-free scenario allows indirect passive localisation, which is relevant for safety and security. At this stage, it is important to mention that the spacing of hydrophones can influence the apparent size and resolution of detected objects, meaning that coarse arrays may miss small or fast-moving targets such as divers, autonomous vehicles or compact remotely operated vehicles. Ideally, a dense hydrophone array would provide the most detailed spatial information, but deploying such a setup is often unaffordable and time-consuming. However, in practice,

DOI: 10.5281/zenodo.17120138

existing hydrophone networks that were originally installed for climate or environmental monitoring purposes can be repurposed, for instance, in regions close to maritime borders.

In conclusion, although OAT has proven highly effective for environmental monitoring and can cover vast areas, its use requires precisely known transmitter and receiver positions, long-term calibration, and inversion of travel times across multiple acoustic paths. Consequently, it cannot deliver rapid real-time threat assessment and should instead be considered a background monitoring layer for early warning in strategic areas near harbours or maritime borders. In these settings, it can complement sonar systems or distributed fibre-optic sensing by providing a detailed ocean model for enhanced target detection. Future work should include extended simulations with a 3D harbour model incorporating more complex wave phenomena, such as bottom and surface reflections, and using a combined FEM–BEM approach with varied object dimensions and hydrophone configurations. While FEM is appropriate for the small-scale harbour model considered here (10 × 12.5 m), real-scale harbour simulations could benefit from RT for computational efficiency, or hybrid approaches (FEM–RT, i.e., FERT) that combine FEM accuracy in critical areas with RT efficiency for the larger domain. Experimental validation and the application of reconstruction algorithms should also be pursued.

Acknowledgments

The presented work is done as a part of master's thesis at the AGH University of Krakow under the guidance of dr hab. inż. Ireneusz Czajka, prof. AGH. The authors would like to express sincere gratitude to AGH University of Krakow for providing access to the COMSOL Multiphysics license, which significantly contributed to the successful completion of this research. The support of the university's facilities and resources is greatly appreciated.

References

[1] D. Zeng *et al.*, "A survey on sensor deployment in underwater sensor networks," in *Advances in Wireless Sensor Networks*, Lecture Notes in Electrical Engineering, pp. 133–143, Berlin, Heidelberg: Springer, 2014.

[2] A. J. Williams, "Innovative technology in oceanography: Past, present and future," in *International Symposium on Ocean Electronics*, pp. 3–17, 2011.

[3] A. P. S. Wong *et al.*, "Argo data 1999–2019: Two million temperature-salinity profiles and subsurface velocity observations from a global array of profiling floats," *Frontiers in Marine Science*, vol. 7, p. 700, 2020.

[4] J. J. Jijesh *et al.*, "Development of a CTD sensor subsystem for oceanographic application," in *IEEE International Conference on Recent Trends in Electronics, Information & Communication Technology (RTEICT)*, pp. 1487–1492, 2017.

[5] J. Gould, B. Sloyan, and M. Visbeck, "Chapter 3 - in situ ocean observations: A brief history, present status, and future directions," in *Ocean Circulation and Climate* (G. Siedler *et al.*, eds.), vol. 103 of *International Geophysics*, pp. 59–81, Academic Press, 2013.

[6] J. D. Hedley *et al.*, "Environmental and sensor limitations in optical remote sensing of coral reefs: Implications for monitoring and sensor design," *Remote Sensing*, vol. 4, no. 1, pp. 271–302, 2012.

[7] V. Sivakumar and D. Rekha, "Underwater acoustic sensor network: Research challenges," *International Journal of Control Theory and Applications*, vol. 9, no. 52, pp. 651–658, 2016.

[8] B. D. Cornuelle, "Acoustic tomography," *IEEE Transactions on Geoscience and Remote Sensing*, vol. GE-20, no. 3, pp. 326–332, 1982.

[9] W. Munk and C. Wunsch, "Ocean acoustic tomography: A scheme for large scale monitoring," *Deep Sea Research Part A. Oceanographic Research Papers*, vol. 26, no. 2, pp. 123–161, 1979.

[10] D. Behringer *et al.*, "A demonstration of ocean acoustic tomography," *Nature*, vol. 299, pp. 121–125, Sept. 1982.

[11] B. Dushaw *et al.*, "Data report: Acoustic mid-ocean dynamics experiment (AMODE)," 1996.

[12] B. D. Dushaw *et al.*, "A decade of acoustic thermometry in the north pacific ocean," *Journal of Geophysical Research: Oceans*, vol. 114, no. C7, 2009.

[13] The ATOC Consortium, "Ocean climate change: Comparison of acoustic tomography, satellite altimetry, and modeling," *Science*, vol. 281, no. 5381, pp. 1327–1332, 1998.

[14] G. D'Antona and R. Ottoboni, "Time of flight measuring system for lakes acoustic tomography," in *Proceedings of the 19th IEEE Instrumentation and Measurement Technology Conference*, vol. 2, pp. 1671–1673, 2002.

[15] A. Kaneko, X.-H. Zhu, and J. Lin, "Chapter 1 - fundamental knowledge," in *Coastal Acoustic Tomography* (A. Kaneko, X.-H. Zhu, and J. Lin, eds.), pp. 1–12, Elsevier, 2020.

[16] B. D. Cornuelle *et al.*, "Ocean acoustic tomography at 1000-km range using wavefronts measured with a large-aperture vertical array," *Journal of Geophysical Research: Oceans*, vol. 98, no. C9, pp. 16365–16377, 1993.

[17] A. Goodney and Y. H. Cho, "Acoustic tomography with an underwater sensor network," in *2012 Oceans*, pp. 1–10, 2012.

[18] B. Taddiken and K. Krock, "66 years of undersea surveillance," *Naval History Magazine*, vol. 35, February 2021.

[19] F. Ihlenburg, *Finite Element Analysis of Acoustic Scattering*, vol. 132 of *Applied Mathematical Sciences*. New York: Springer-Verlag, Aug. 1998.

[20] D. R. Bergman, *Computational Acoustics: Theory and Implementation*. Applied Acoustics and Vibration, New York: Wiley-Blackwell, 1 ed., 2017.

[21] S. Kirkup, *The Boundary Element Method in Acoustics*. Southampton, UK: Integrated Sound Software, 2007.

[22] J. M. Hovem, "Ray trace modeling of underwater sound propagation," in *Modeling and Measurement Methods for Acoustic Waves and for Acoustic Microdevices* (M. G. Beghi, ed.), ch. 23, Rijeka: IntechOpen, 2013.

[23] A. Krokstad, U. P. Svensson, and S. Strøm, "The early history of ray tracing in acoustics," in *Acoustics, Information, and Communication: Memorial Volume in Honor of Manfred R. Schroeder*, vol. 916 of *Lecture Notes in Physics*, pp. 15–31, Cham, Switzerland: Springer, 2015.

[24] I. Jovanović, *Inverse Problems in Acoustic Tomography: Theory and Applications*. PhD thesis, École Polytechnique Fédérale de Lausanne, Lausanne, Switzerland, 2008.

[25] C. Othmani *et al.*, "Acoustic tomographic reconstruction of temperature and flow fields with focus on atmosphere and enclosed spaces: A review," *Applied Thermal Engineering*, vol. 223, p. 119953, 2023.

[26] J. Gregor and T. M. Benson, "Computational analysis and improvement of (SIRT)," *IEEE Transactions on Medical Imaging*, vol. 27, no. 7, pp. 918–924, 2008.

[27] G. Fischer, M. Starke, and A. A. Ziemann, "Acoustic tomography of the atmosphere: Comparison of different reconstruction algorithms," *Acta Acustica united with Acustica*, vol. 98, no. 4, pp. 534–545, 2012.

[28] Y. Bao and J. Jia, "Nonlinear temperature field reconstruction using acoustic tomography," in *IEEE International Symposium on Thermophysics (IST)*, pp. 1–6, 2017.

[29] A. Pourmohammad and S. M. Ahadi, "N-dimensional n-microphone sound source localization," *EURASIP Journal on Audio, Speech, and Music Processing*, vol. 2013, no. 27, 2013.

[30] H. A. H. Catur and H. M. Saputra, "Azimuth estimation based on generalized cross correlation phase transform (gcc-phat) using equilateral triangle microphone array," in *2019 International Conference on Radar, Antenna, Microwave, Electronics, and Telecommunications (ICRAMET)*, pp. 89–93, 2019.

DOI: 10.5281/zenodo.17120138